ARMY RESEARCH LABORATORY

Navier-Stokes Predictions of Dynamic Stability Derivatives: Evaluation of Steady-State Methods

by James DeSpirito, Sidra I. Silton, and Paul Weinacht

ARL-TR-4605 **September 2008**

NOTICES

Disclaimers

The findings in this report are not to be construed as an official Department of the Army position unless so designated by other authorized documents.

Citation of manufacturer's or trade names does not constitute an official endorsement or approval of the use thereof.

Destroy this report when it is no longer needed. Do not return it to the originator.

Army Research Laboratory
Aberdeen Proving Ground, MD 21005-5066

ARL-TR-4605 **September 2008**

Navier-Stokes Predictions of Dynamic Stability Derivatives: Evaluation of Steady-State Methods

James DeSpirito, Sidra I. Silton, and Paul Weinacht
Weapons and Materials Research Directorate, ARL

REPORT DOCUMENTATION PAGE	Form Approved OMB No. 0704-0188

1. REPORT DATE *(DD-MM-YYYY)*	2. REPORT TYPE	3. DATES COVERED (From - To)
September 2008	Final	January 2007–December 2007

4. TITLE AND SUBTITLE
Navier-Stokes Predictions of Dynamic Stability Derivatives: Evaluation of Steady-State Methods

5a. CONTRACT NUMBER

5b. GRANT NUMBER

5c. PROGRAM ELEMENT NUMBER

6. AUTHOR(S)
James DeSpirito, Sidra I. Silton, and Paul Weinacht

5d. PROJECT NUMBER
62618AH80

5e. TASK NUMBER

5f. WORK UNIT NUMBER

7. PERFORMING ORGANIZATION NAME(S) AND ADDRESS(ES)
U.S. Army Research Laboratory
ATTN: AMSRD-ARL-WM-BC
Aberdeen Proving Ground, MD 21005-5066

8. PERFORMING ORGANIZATION REPORT NUMBER
ARL-TR-4605

9. SPONSORING/MONITORING AGENCY NAME(S) AND ADDRESS(ES)

10. SPONSOR/MONITOR'S ACRONYM(S)

11. SPONSOR/MONITOR'S REPORT NUMBER(S)

12. DISTRIBUTION/AVAILABILITY STATEMENT
Approved for public release; distribution is unlimited.

13. SUPPLEMENTARY NOTES

14. ABSTRACT
The prediction of the dynamic stability derivatives—roll-damping, Magnus, and pitch-damping moments—were evaluated for three spin-stabilized projectiles using steady-state computational fluid dynamic (CFD) calculations. Roll-damping CFD predictions were found to be very good across the Mach number range investigated. Magnus moment predictions were very good in the supersonic flight regime; however, the accuracy varied in the subsonic and transonic flight regime. The best Magnus moment prediction in the subsonic flight regime was for the square-base projectile that did not exhibit highly nonlinear Magnus moments. A primary contribution of this report is the demonstration that the pitch-damping moment can be adequately predicted via steady-state methods rather than resorting to unsteady techniques. The predicted pitch-damping moment compared very well to experimental data for the three projectiles investigated. For one configuration, the pitch-damping moment was predicted by several CFD codes, two different steady-state methods, and a time-accurate planar pitching motion method. All methods compared very well to each other and to the experimental data.

15. SUBJECT TERMS
dynamic stability, computational fluid dynamics, aerodynamics, pitch damping, roll damping, Magnus, acoustics, level-dependent earplugs

16. SECURITY CLASSIFICATION OF:			17. LIMITATION OF ABSTRACT	18. NUMBER OF PAGES	19a. NAME OF RESPONSIBLE PERSON
a. REPORT	b. ABSTRACT	c. THIS PAGE			James DeSpirito
UNCLASSIFIED	UNCLASSIFIED	UNCLASSIFIED	UL	44	19b. TELEPHONE NUMBER (*Include area code*) 410-306-0778

Standard Form 298 (Rev. 8/98)
Prescribed by ANSI Std. Z39.18

Contents

List of Figures

List of Tables

Acknowledgments

The authors thank Dr. Daniel Corriveau of the Defence Research and Development Canada – Valcartier, for supplying additional 0.50-cal. aeroballistic range test data and obtaining permission for us to publish under the auspices of the Technical Cooperation Program. This work was supported in part by a grant of high-performance computing time from the U.S. Department of Defense High Performance Computing Modernization program at the U.S. Army Research Laboratory Major Shared Resource Center, Aberdeen Proving Ground, MD.

INTENTIONALLY LEFT BLANK.

1. Introduction

Computational fluid dynamic (CFD) calculations to accurately predict the static aerodynamic coefficients (e.g., drag, longitudinal, and lateral forces and moments) and flow phenomena of many geometrically complex, single-body and multibody projectiles and missiles are routinely used by many investigators using commercial and Government-sponsored CFD software packages. The prediction of dynamic coefficients such as pitch-damping, roll-damping, and Magnus moments has not achieved widespread use, even though some methods for efficient prediction via steady-state methods (e.g., for pitch damping) were demonstrated over 10 years ago (*1–6*). To determine the full set of static and dynamic aerodynamic data needed to predict projectile in-flight motion, projectile designers still turn to flight tests (both aeroballistic range and telemetry free-flight) as their primary source for dynamic aerodynamic coefficients. If CFD can be proven to efficiently provide accurate dynamic data, in addition to the static aerodynamics, it would be a great benefit to munition designers.

The prediction of dynamic aerodynamics is inherently more difficult than the basic static coefficients. However, with the computational resources, CFD solver techniques, and other advances available today, there are viable solutions to the problem. It is desired that the prediction methods are "efficient" enough (e.g., steady-state rather than time-accurate methods when possible; reduced mesh sizes when possible, etc.) to limit the computation time to reasonable levels in order to impact the design phase of development programs. The results of recent work by many investigators on time-accurate CFD methods to predict dynamic coefficients are promising, but it can be computationally expensive in time and computer resources (*7–11*). The method of Sahu (*11*, *12*) is based on a time-accurate, coupled CFD and rigid body dynamics approach that is the equivalent to simulating the projectile flight through an aeroballistic spark range. While this latter method is potentially the most robust, it is very computation intensive and the accuracy of the dynamic stability derivatives may be limited to the accuracy of those available from spark range data, since the same type of curve fit data reduction methods are used to back out the aerodynamic coefficients.

The prediction of Magnus force and moment of spin-stabilized projectiles via steady-state CFD methods was demonstrated in the supersonic and high transonic regimes in early investigations (*13–15*). However, that work was limited in scope due to computational resources. Recent work by U.S. Army Research Laboratory (ARL) investigators indicates that the prediction of Magnus via steady-state methods in the subsonic and low transonic regime may not be as accurate as those in the supersonic regime, at least for some projectile base shapes (*16–18*). Time-accurate CFD with advanced turbulence approaches (e.g., hybrid Reynolds-average Navier-Stokes [RANS] and Large-Eddy Simulation [LES]) showed improved Magnus predictions (*17*, *18*).

Roll-damping coefficients are usually adequately predicted via steady-state computations (*16–18*). Weinacht et al. (*1–4*) showed success in predicting pitch damping of axisymmetric and finned projectiles in the transonic through supersonic Mach number range using a steady-state solution method with the projectile undergoing a coning motion.

This report presents the results of several spin-stabilized projectiles of various calibers. The U.S. Army-Navy Spinner Rocket (ANSR), the 25-mm M910 subcaliber projectile, and the 0.50-cal. projectile are included in this study. The steady-state pitch-damping results for the ANSR are also compared to unsteady methods. The pitch-damping prediction results from several CFD codes are also compared for the ANSR. In addition, this report hopes to demonstrate that all the dynamic stability derivatives of most spin-stabilized projectiles can be adequately predicted via steady-state CFD methods. The CFD prediction capabilities of Magnus moment in the subsonic and transonic flight regimes is still somewhat of an issue and is discussed elsewhere (*18, 19*).

2. Numerical Approach

2.1 U.S. Army-Navy Spinner Rocket (ANSR)

The computational model of the 7-cal. (1 cal. = 20 mm) ANSR is shown in figure 1. The ANSR consists of a 2-cal. secant ogive followed by a 5-cal. cylindrical afterbody. Three center of gravity (c.g.) locations were investigated: 3.250, 4.036, and 4.818 cal. from the nose.

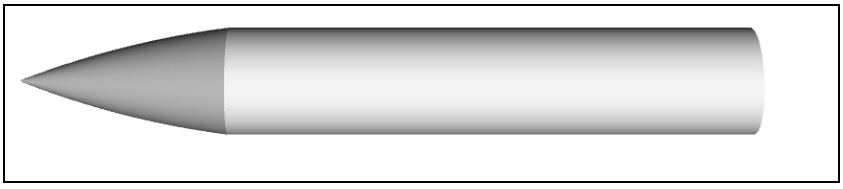

Figure 1. A 7-cal. ANSR model with square base.

2.1.1 CFD++ Simulations

The geometry and unstructured mesh were generated using GAMBIT, a geometry and grid preprocessor supplied with the FLUENT CFD software suite (*20*). A full three-dimensional (3-D) mesh was required in all cases to simulate the spinning shell at angle of attack. In generating the meshes, boundary layer mesh spacing was used near the projectile body. Resolving the viscous boundary layer is critical for predicting the Magnus and roll-damping moments; therefore, wall functions were not used, instead using the option to integrate the equations to the wall. Normally a y^+ value on the order of 1.0 is adequate to resolve the

boundary layer. However, it was desired to have a y^+ value of 0.5 or less to ensure capturing the Magnus effect of the spinning shell. All mesh stretching ratios were kept to 1.2 or less.

One mesh was generated for the Mach number *(M)* range of $0.7 < M < 2.5$ and is shown in figure 2. An unstructured mesh consisting of 3.4 M hexagonal cells was used. An O-grid mesh was generated around the projectile body to contain the dense viscous mesh required to resolve the boundary layer. This O-grid extended to a distance of 0.1 cal. from the projectile body. A C-grid type mesh was then generated around the body to a distance of 0.5 cal. from the projectile body. The C-grid mesh was extended from the base of the projectile to the rear boundary of the computational domain. The region ahead of the projectile was meshed with a mapped-type mesh. The remainder of the computational domain was meshed with hexagons generated by revolving the paved quads around the axis (this is a Cooper mesh in GAMBIT). The computational domain extended for 35 cal. in front of the model and 50 cal. radially and behind the model. A grid resolution study performed as part of another study (*19*) showed that the mesh resolution was adequate. Time-accurate RANS/LES simulations were later performed (*19*) on the ANSR configuration using a finer mesh in the wake region. The size of that mesh was about 3× the size of that used in the RANS simulations.

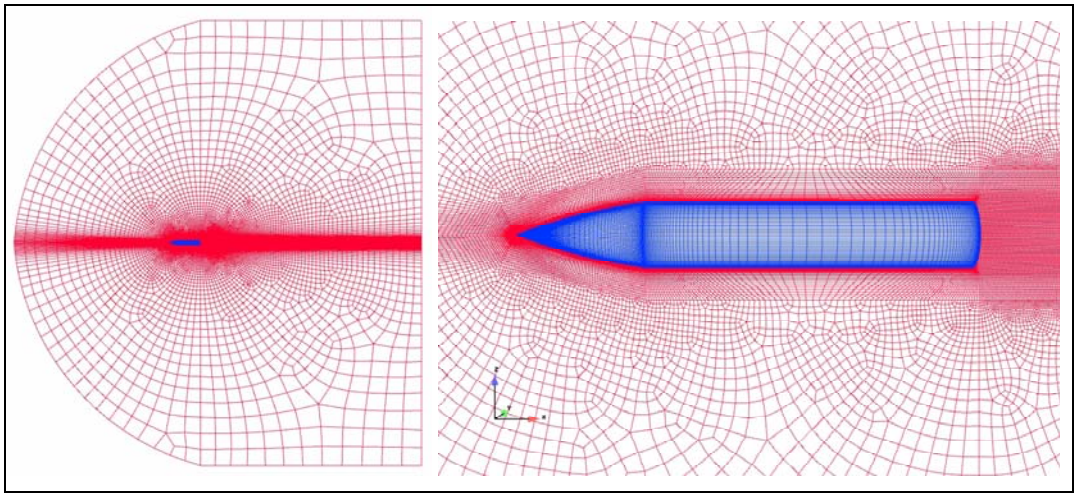

Figure 2. Computational mesh used for 7-cal. ANSR model in CFD++ simulations.

The outer boundaries were set to free-stream conditions at standard sea level temperature and pressure (101.325 kPa, 288 K). The projectile wall was modeled as a no-slip, isothermal (288-K) wall boundary, rotating (clockwise when viewed from rear) around the x-axis at the specified spin rate. The projectile spin rates were determined from the muzzle exit twist of 10 cal. per revolution (*21*), corresponding to a muzzle exit, nondimensional spin rate (*pd/2V*) of 0.315.

The commercially available CFD^{++} code (*22*) version 6.1.1, was used in this study. The CFD^{++} code can simulate a range of fluid dynamic phenomena, ranging from incompressible to hypersonic flow. The 3-D, time-dependent, RANS equations are solved using the finite volume method. The implicit solver with dual time-stepping was used. The spatial discretization was a second-order, multidimensional TVD (total variation diminishing) polynomial interpolation scheme. Solutions to semi-infinite "Riemann problems" are used in CFD^{++} to provide upwind flux information to the underlying transport scheme. Approximate Riemann solvers are used to determine the higher order fluxes to avoid spurious oscillations that may become physically unbounded if determined via fixed-stencil interpolation.

The three-equation k-ε-R model, which solves transport equations for the turbulence kinetic energy, k, its dissipation rate, ε, and the undamped eddy viscosity, R, was used. This model was previously found to provide good performance across the subsonic through supersonic Mach number range (*17*). CFD^{++} also has available LES models and hybrid RANS/LES models, including the Detached-Eddy Simulation model.

Most of the simulations were performed in parallel on an 1100-node, 4400-core, Linux Networx Advanced Technology Cluster at the U.S. ARL Major Shared Resource Center. Each node has two dual-core 3.0-GHz Intel Woodcrest processors. Some simulations were performed on an older 1024-node, Linux Networx Evolocity II system with two 3.6-GHz Intel Xeon EM64T processors per node. The number of processors used for each run was such that about 145,000–150,000 cells were partitioned on each processor. The calculations took about 11–15 s of CPU time per iteration and convergence was achieved in about 600–800 iterations. The solution was deemed converged when the flow residuals had reduced at least 3 orders of magnitude and the aerodynamic coefficients changed less than about 0.5% over the last 100 iterations. The aerodynamic coefficients were the determining factor in convergence in all cases.

The double precision solver with second-order spatial discretization was used. The maximum Courant-Friedrich-Lewy (CFL) number was chosen using the recommendations within the CFD^{++} solver; e.g., for the transonic flow regime ($0.7 < M < 1.4$), the CFL number is ramped from 1 to 75.0 over the first 100 iterations.

2.1.2 Overflow 2 Simulations

The flow field about the 7-cal. ANSR was also predicted through an overset grid approach using the NASA code Overflow 2 (*23–25*). The method uses a near-body grid system of interconnecting grids that conform to various parts of the body surrounded by an outer, off-body Cartesian-based grid system (figure 3). The interconnecting near-body grids overlap and intergrid connectivity is established using a Chimera overset gridding approach. This significantly reduces the demands on grid generation of complex shapes, as each body component can be gridded independently. The outer off-body Cartesian grid system encompasses the near-body grid system and extends to the outer boundary of the computational domain. The off-body grid system typically consists of several levels of grid refinement, with

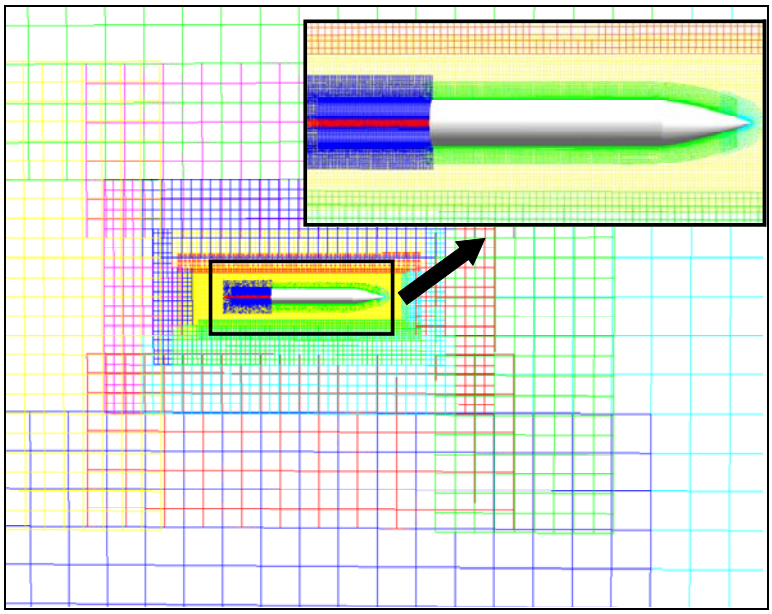

Figure 3. Overset grids used in Overflow 2 ANSR computations.

the most refined grids in proximity to the near-body grids and increasingly less refined grids further away from the body.

Solution of the compressible RANS equations was accomplished using a three-factor diagonal-implicit, first-order accurate time-stepping scheme that employs second-order accurate central differencing in space. The Baldwin-Barth (*26*) one-equation turbulence model was used. Characteristics based inflow/outflow boundary conditions have been applied on the boundaries of the domain. On the body surface, no-slip, adiabatic boundary conditions were imposed. The code was modified for use in the current study; including the addition of a tangential velocity boundary condition to account for the rigid-body rotation due to spin and the addition of the rotating coordinate frame source terms and associated outer boundary conditions required for the coning motion computations.

In addition to steady coning computations, the Overflow 2 code was also used to solve for pitch damping using a planar pitching motion. Typically, a simple constant-amplitude sinusoidal pitching motion is used (*9*, *10*), although other types of motion can be applied (*27*). This type of computation must be performed as a time-accurate calculation since imposed motion generates an unsteady, though periodic, flow field.

For the planar pitching motion computations, the grid motion was specified through the use of a general interface (*28*), which was implemented in the distributed version of the Overflow 2 code. This replaced the need for hard coding of the motion that had been required in earlier work using prior generations of the code. The time-dependent computations were accomplished using a body-fixed, rotating, near-body computational mesh that rotates relative to the stationary outer off-body Cartesian grid system. During the course of the investigation, it was determined that

inner iterations at each time step were required to obtain a suitably converged solution. Five to twenty inner iterations were required to obtain a converged solution for the planar pitching motion computations with more inner iterations required at the transonic and subsonic velocities. Global integrated force/moment data was obtained from the computed flow fields using the FOMOCO utility (*29*). Force and moment distributions along the body were also obtained from the computed flow fields through minor modifications to the existing code and additional auxiliary postprocessing tools.

The time dependent variation of the pitching moment was computed for multiple cycles of the pitching motion. To speed the planar pitching motion computations, a nondimensional pitching rate of 0.05 was used. Computations were performed at lower pitching rates to confirm the independence of the results to angular rate. The computations were initiated from a zero angle-of-attack, steady-state solution. After about a quarter cycle of motion, the computed pitching moment displayed a periodic behavior that repeated itself with subsequent cycles of motion.

2.2 The 25-mm M910

The M910 target-practice discarding-sabot, traced (TPDS-T) subprojectile is shown in figure 4. The aluminum nose consists of a 0.22-cm meplat, followed by a 4.12-cm conical ogive. The ogive is followed by a cylindrical, steel body that is 3.27 cm long with a diameter of 1.62 cm (1 cal.). A 0.2-cm chamfer forms the base of the projectile. The c.g. is located 4.99 cm (3.08 cal.) from the nose.

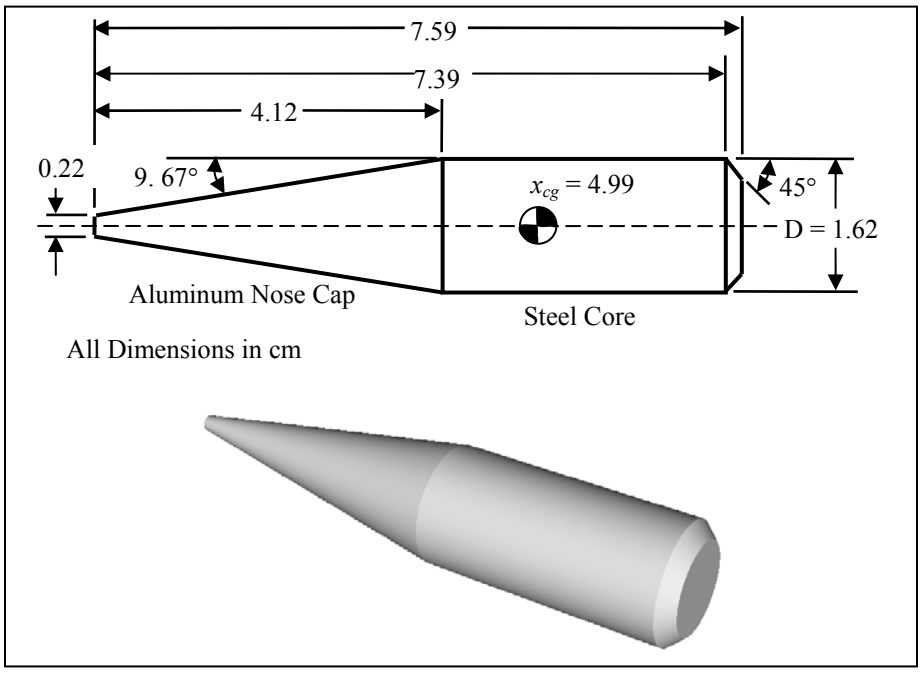

Figure 4. Schematic and computational model of the 25-mm M910 TPDS-T subprojectile.

The geometry and unstructured mesh were generated using GAMBIT following the same methodology as for the ANSR model. Two meshes were used for the steady-state CFD calculations in this study; one for supersonic calculations ($M > 1.4$), and one for subsonic and transonic calculations ($M \leq 1.4$). A grid resolution performed as part of an earlier study (*17*) showed that the current meshes were adequate for the steady-state computations.

The properties of the meshes are compared in table 1, including the location of the outer boundary of the computational domain with respect to the projectile. The near-body region of all meshes was similar figure 5, with the subsonic/transonic mesh generated by making another mesh around the supersonic mesh. An O-grid was manually generated around the projectile body, building a boundary layer mesh off the entire projectile surface. The circumferential direction contained 136 cells. Also shown in table 1 are the mesh characteristics for the time-accurate RANS/LES calculations (*18*). The higher resolution mesh required in the wake region increases the total mesh size about 3× that required for standard steady-state simulations.

Table 1. M910 computational mesh characteristics.

Case	Number Cells	Radial Boundary (cal.)	Front Boundary (cal.)	Rear Boundary (cal.)	First Boundary Layer Edge (cal.)
RANS supersonic	1,952,480	3.51	0.31	5.31	1.54×10^{-5}
RANS subsonic	1,960,928	45.8	24.7	39.8	4.00×10^{-5}
RANS/LES supersonic	5,412,752	3.51	0.31	39.8	1.54×10^{-5}
RANS/LES subsonic	5,997,512	45.8	24.7	39.8	4.00×10^{-5}

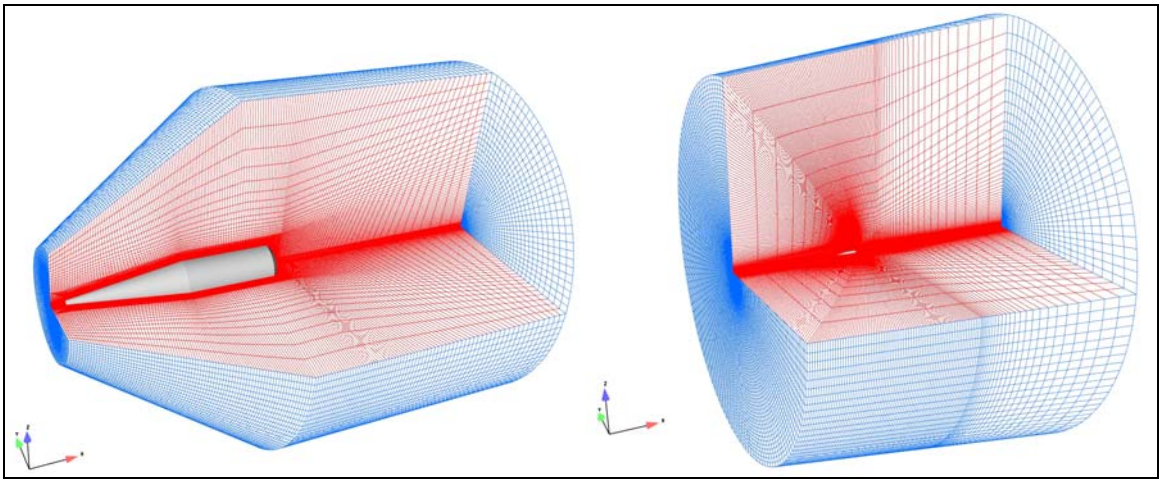

Figure 5. Computational mesh for supersonic cases ($M > 1.4$) and subsonic/transonic cases ($M \leq 1.4$).

The boundary conditions were set the same as for the ANSR model: free-stream outer boundaries set to standard sea level temperature and pressure (101.325 kPa, 288 K), and no-slip, isothermal (288-K) wall boundary rotating at specified spin rate. The projectile spin rates were determined from the muzzle exit twist of the M242 gun (23.9 cal. per revolution). The muzzle exit nondimensional spin rate in this case is 0.131. CFD++ v6.1.1 was also used in the M910 study and the solution methodology was that same as that used in the ANSR study.

2.3 The 0.50-cal. Projectile

The computational model of the 0.50 cal. (1 cal. = 12.95 mm) projectile is shown in figure 6. The projectile is 4.46 cal. long, with a 0.16 cal. long by 0.02 cal. deep groove, and a 9° filleted boattail. The center of gravity location is 2.68 cal. from the projectile nose. The projectile spin rates were determined from the muzzle exit twist rate, 29.42 cal. per revolution (*30*), which gives the nondimensional spin rate of 0.107. The meshes used in the 0.50-cal. projectile study were 3-D unstructured (hexahedrals, pyramids, and tetrahedrals) meshes created using GRIDGEN Version 15 software (*31*).

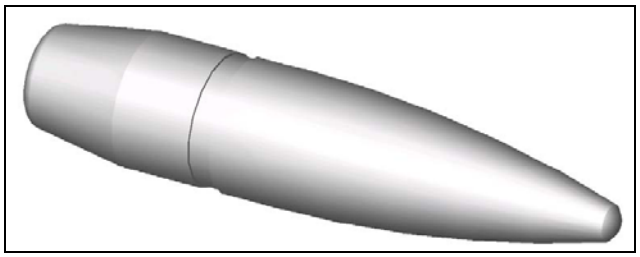

Figure 6. A 0.50-cal. projectile computational model.

Several separate meshes were constructed over the course of the original 0.50-cal. projectile study (*16*). The meshes included one for subsonic and low supersonic cases, one for a near-sonic case, and two for supersonic cases. The last two grids were created in order to verify grid independence (*16*). Two new meshes were created for the current study using the previous grids as guidance; one for supersonic flow ($M > 1.5$) and one for transonic and subsonic ($M \leq 1.5$). The properties of the two meshes, including the location of the outer boundary relative to the body, are given in table 2. These meshes were generated with a more resolved wake region appropriate for time-accurate RANS/LES simulations and are about twice the size as those in the original 0.50-cal. projectile study (*16*) .

Table 2. A 0.50-cal. projectile computational mesh characteristics.

Case	Number Cells	Radial Boundary (cal.)	Front Boundary (cal.)	Rear Boundary (cal.)	First Boundary Layer Edge (cal.)
Supersonic	5,905,658	5.3	5.8	14.9	1.9×10^{-5}
Subsonic	7,216,576	89.9	90.3	89.4	5.6×10^{-5}

The near-body region of both meshes was similar, with the subsonic mesh generated by making another mesh around the supersonic grid. Figure 7 shows two views of the subsonic mesh: the complete subsonic mesh and a close-up showing the limits of the supersonic mesh. Each mesh contained 144 circumferential cells. An O-grid was generated around the body (0.57 cal. away) using the hyperbolic extrude feature with GRIDGEN. The grid generation characteristics, computational domain, boundary conditions, and simulation approach using CFD++ were similar to those for the ANSR and M910 studies described earlier.

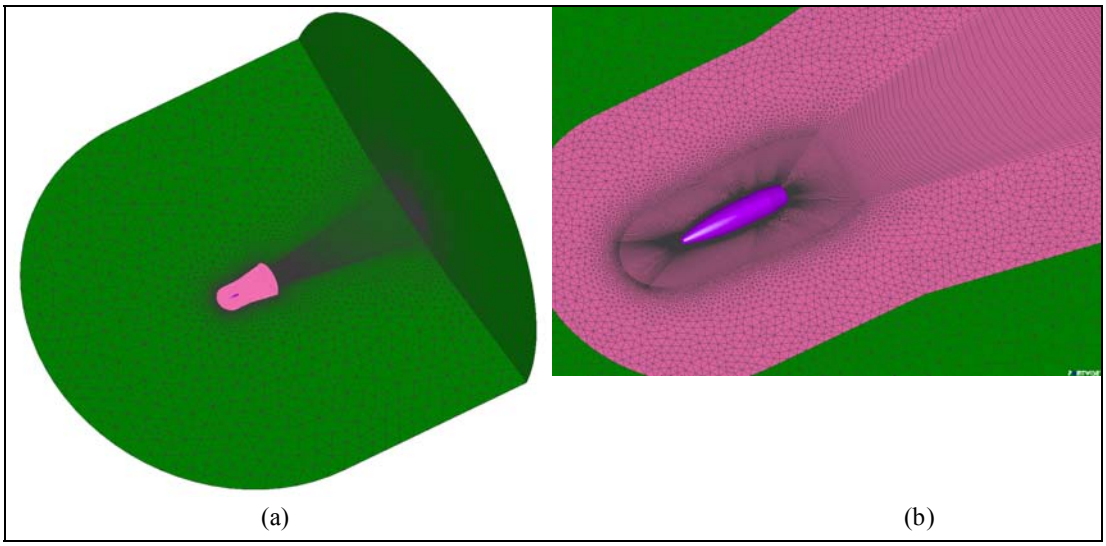

Figure 7. Typical computational meshes for 0.50-cal. projectile: (a) subsonic mesh (extent of supersonic mesh shown in pink) and (b) close-up of supersonic mesh around which subsonic mesh was built.

3. Pitch-Damping Calculation

3.1 Steady Coning Methodology

The pitch-damping coefficient sum calculation follows the procedures described by Weinacht et al. (*1*) for axisymmetric bodies. Their approach uses a specific combination of steady-state spinning and coning motions that allows the pitch-damping force and moment coefficient to be directly related to the aerodynamic side force and moment within given constraints. The constraints are that the coning rate and the angle of attack must be small. The flow may become unsteady at high coning rates or high angles of attack in much the same way the flow over a body at fixed angle of attack at high incidence can become unsteady due to vortex shedding. Weinacht et al.'s (*1*) use of the combined spinning and coning motion was an improvement over previous techniques that simply used a lunar coning motion (no prescribed rotation about the

projectile axis) for prediction of the pitch-damping coefficients. In both cases, the projectile axis is oriented at a constant angle with respect to the free-stream velocity vector, as shown in figure 8.

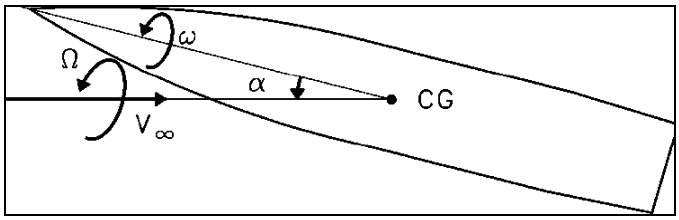

Figure 8. Schematic of coning motion.

The aerodynamic side force and moment coefficients acting on a projectile in steady coning motion can be related to the pitch-damping force and moment coefficients. In steady coning motion, the longitudinal axis of the projectile performs a rotation at a constant angular velocity about a line parallel to the free-stream velocity vector and coincident with the projectile c.g. In steady lunar coning motion, the angular velocity of the projectile results purely from the rotation, Ω, of the projectile about the free-stream velocity vector. The angular velocity includes a component along the projectile's longitudinal axis, which by definition is the spin rate of the projectile in the nonrolling coordinate system (*1*), $p = \dot{\phi}\cos\alpha_t = \dot{\phi}\gamma$, where $\alpha_t = \sqrt{\alpha^2 + \beta^2}$. In the combined spinning and coning motion, the angular velocity of the projectile is the vector sum of two angular velocity vectors. The first vector produces a rotation of the projectile axis about the free-stream velocity vector (coning motion) $\dot{\phi}$, and the second produces a rotation of the projectile about its longitudinal axis (spinning motion) ω. There is no general requirement that the spin rate be coupled to the coning rate. However, in this analysis, the combined spinning and coning motion requires that ω be equal in magnitude but opposite in sign to the component of $\dot{\phi}$ along the longitudinal axis, $\omega = -\dot{\phi}\gamma$. The total angular velocity of the body about the longitudinal axis is zero, and the spin rate in the nonrolling coordinate system is zero: $p = 0$. Hence, the projectile angular motion is completely defined once the coning rate and the spin rate are specified.

The appeal of both of these methods is that only steady-state computations are required. In both methods, the motion can be decomposed into a combination of two orthogonal planar pitching motions. For steady lunar coning motion, there is no rotation of the pitch plane with respect to the body, while the case of combined coning and spinning includes a rotation around the body axis. The boundary conditions in the coning frame do not introduce any time dependency into the problem when observed from the coning reference frame, so the resulting flow field is expected to be steady for small angles of attack and small coning rates. Because the coning frame is rotating at a constant angular velocity, and the body does not rotate with respect to the coning reference frame, there is no requirement of axisymmetry for steady flow to exist (*4*).

The case of steady combined spinning and coning motion is different, since the body will rotate in the coning reference frame at a rate of rotation that is proportional to the coning rate, $\omega = -\dot{\phi}\cos\alpha_t$. This rotation does not produce a time-dependent boundary condition for axisymmetric bodies, thus, steady flow exists. However, for nonaxisymmetric bodies, the rotation of the body in the coning reference frame will produce a time-dependent (periodic) boundary condition in the flow field, making the combined spinning and coning method appropriate only for axisymmetric bodies.

The detailed relationship between the side moment due to coning motion and the pitch-damping moment coefficient developed by Weinacht et al. (*1*) is summarized here. Note the dynamic coefficients were nondimensionalized by $\dot{\phi}d/V$ in previous work (*1–4*), while here the convention of $\dot{\phi}d/2V$ is used. The moment formulation cast in terms of the in-plane and side moments is written as follows:

$$C_m + iC_n = C_{m_\alpha}\delta + i\left\{\left(\frac{\dot{\phi}\gamma d}{2V}\right)C_{n_{p\alpha}}\delta + \delta\left(\frac{\dot{\phi}d}{2V}\right)\left[C_{m_q} + \gamma C_{m_{\dot{\alpha}}}\right]\right\}. \tag{1}$$

The in-plane moment (real part) results only from the pitching moment, while the total side moment (complex part) consists of contributions from the Magnus moment and the pitch-damping moment. For lunar coning motion, the side moment can be written as follows:

$$C_n = \delta\left(\frac{\dot{\phi}d}{2V}\right)\left(\gamma C_{n_{p\alpha}} + \left[C_{m_q} + \gamma C_{m_{\dot{\alpha}}}\right]\right), \tag{2}$$

with the Magnus component due to the component of angular velocity along the longitudinal axis of the projectile. The right-hand side of equation 2 is simply the variation of side moment with coning rate, as shown in the following:

$$C_{n_{\dot{\phi}}} \equiv \frac{\partial C_n}{\partial\left(\dot{\phi}d/2V\right)} = \delta\left(\gamma C_{n_{p\alpha}} + \left[C_{m_q} + \gamma C_{m_{\dot{\alpha}}}\right]\right). \tag{3}$$

For bodies of revolution, a single computation at a nonzero coning rate is sufficient because the side moment for a projectile with zero coning rate is zero.

In the case of combined spinning and coning motion the spin rate of the projectile, as observed from the nonrolling coordinates, is zero. In the coning coordinate frame, the body will spin in the opposite direction of the coning motion, i.e., $\omega = -\dot{\phi}\gamma$, thereby canceling the induced spin rate due to coning motion. For this motion, the side moment can be written as follows:

$$C_n = \delta\left(\frac{\dot{\phi}d}{2V}\right)\left[C_{m_q} + \gamma C_{m_{\dot{\alpha}}}\right]. \tag{4}$$

In this case, the side moment is directly proportional to the pitch-damping moment coefficient and no Magnus term appears in the equation. As noted by Weinacht et al. (*1*), even when using

the combined spinning and coning motion and equation 4, the Magnus effect has not been entirely removed from the problem. For example, in the coning frame, the combination of angle of attack from the coning motion and spinning motion produce a Magnus-like effect that must be resolved by the CFD computations (i.e., the near-body mesh resolution must be adequate to resolve the boundary layer modification due to the Magnus effect). Many projectile and missile applications deal with small amplitude motions, therefore, it is customary to linearize the equations of motion. In this case, the cosine of the angle of attack, $\gamma \approx 1$, and the pitch-damping moment appears as $\left(C_{m_q} + C_{m_{\dot{\alpha}}}\right)$.

3.2 Transient Planar Motion Methodology

A variety of approaches exists for processing the computed time-dependent force and moment data to extract the pitch-damping force and moment from the planar pitching motion (*7–11*). In the current effort, the total normal force and pitching moment are assumed to have the functional dependence consistent with a linear force and moment expansion. When simplified for the case of planar pitching motion, the total pitching moment has the form shown in equation 5. A similar expansion exists for the force coefficient, as shown in the following:

$$C_m = C_{m_\alpha} \sin\alpha + \left(C_{m_q} + C_{m_{\dot{\alpha}}}\right) \frac{\dot{\alpha} D}{2V} \ . \tag{5}$$

The angle of attack and angular rate are determined from the sinusoidal variation, as shown in the following:

$$\alpha = \alpha_0 \sin\left(\dot{\alpha}_0 t\right) \ . \tag{6}$$

A least-square fitting process is used to determine coefficients C_{m_α} and $\left(C_{m_q} + C_{m_{\dot{\alpha}}}\right)$ using a series of predicted total pitching moments obtained at two or more independent angles and angular rates. The same procedure is used to extract the normal force and pitch-damping force coefficients. For the results presented here, the predicted total normal force and pitching moment were well represented by the assumed form once the initial transients from the initiation of the planar pitching motion damped out. Data from an entire cycle of motion was used to obtain the pitch-damping coefficients in the results presented here. Although it was determined that data from a portion of the yawing cycle was sufficient to accurately determine the pitch-damping coefficient, data from the full cycle of motion was obtained to ensure the assumed form properly represented the aerodynamic behavior across the range of angle of attack for the computation.

4. Results and Discussion

4.1 Pitch-Damping Calculations

The CFD computations to calculate pitch-damping coefficients are separate from those used to calculate the other aeroballistic coefficients. In the CFD++ computations, the origin of the computational domain is moved to the projectile c.g. and then rotated in the pitch-plane by the coning angle, typically 2° or 3°. For the pitch-damping computations, the computational domain is set to rotate about the *x*-axis—which is no longer the projectile longitudinal axis—at the coning rate, using a rotating reference frame methodology to perform the steady-state computation. The steady-state, rotating-reference frame methodology implemented in CFD++ limited the analysis to lunar coning, since a separate spinning boundary condition about an arbitrary axis could not be appropriately used in conjunction with the rotating reference frame. The results shown in the following sections for the M910 and 0.50-cal. projectiles were all calculated using CFD++ and the steady-state lunar coning method. For the ANSR case, in addition to lunar coning predictions with CFD++, results are also shown for steady-state combined coning-spinning using Overflow 2 and a parabolized Navier-Stokes (PNS) code and the transient planar pitching motion using Overflow 2.

The Magnus force and moment are small in relation to the pitch-damping coefficients and usually can be ignored when using the lunar coning motion. However, the computed Magnus moment coefficients are available from the steady-state computations of the projectile variation with angle of attack and Mach number. Those values of Magnus moment coefficient can be used in equation 3 to compute the pitch-damping coefficients. Although the induced spin rates due to lunar coning are much smaller than those used in the computations of Magnus moments, the Magnus moment coefficient was found in this and previous studies (*1*) to be relatively insensitive to spin rate. Table 3 shows a comparison of the corrected and uncorrected values of pitch-damping moment for the M910 projectile. The "corrected" values were obtained by subtracting the Magnus moment obtained during the static aerodynamic coefficient calculations (i.e., stationary reference frame, nonzero angle of attack, and rotating surface boundary condition on projectile surface). The largest difference is about 2.6% at the lower Mach numbers, showing that neglecting the Magnus term does not incur a large error. However, the Magnus term is easily obtained from the other steady-state calculation and should be used to obtain the correct pitch-damping moment. Note the issue of the accuracy of the steady-state computation of Magnus moment does not affect the correction to the pitch-damping term. The value calculated from the steady-state computation of Magnus moment is used since the coning motion is also a steady-state computation.

Table 3. Comparison of corrected and uncorrected pitch damping values for M910.

Mach No.	$\left[C_{m_q} + C_{m_{\dot{\alpha}}}\right]$ (Corrected)	$C_{n_{p\alpha}} + \left[C_{m_q} + C_{m_{\dot{\alpha}}}\right]$ (From Equation 3)	Percent Difference
0.60	–6.34	–6.50	2.52
0.70	–5.59	–5.74	2.66
0.90	–9.17	–9.26	1.02
0.98	–11.99	–11.98	–0.05
1.02	–11.41	–11.42	0.05
1.20	–14.00	–13.87	–0.95
1.40	–13.74	–13.56	–1.32
2.00	–13.05	–12.87	–1.36
2.50	–12.22	–12.08	–1.14
3.50	–16.50	–16.40	–0.64
4.50	–15.66	–15.57	–0.56

Before presenting the results for the three projectile configurations, several checks of the pitch-damping calculation via the steady lunar coning method are presented. Figure 9a shows the variation of the side moment due to coning with coning rate, equation 2, for two Mach number and three nondimensional coning rates, $\Omega d/2V = 0.0025$, 0.005, and 0.010. The trend lines through the three data points show a very linear trend with a zero intercept, as it should be since Magnus effect is zero at zero spin rate. The slope of the side force curve is equal to the right-hand side of equation 3. The calculations using CFD++ in the following sections were performed with $\Omega d/2V = 0.005$ at a coning angle of 2° or 3°. The combined spinning and coning motion results using Overflow 2 and the PNS code were obtained for coning angles of 2° and $\Omega d/2V = 0.0005$, 0.005, and 0.05. In general, there was little variation in the predicted pitch-damping moment coefficient across the coning rates examined.

Figure 9b shows the variation of this side moment slope with angle of attack for two Mach numbers and $\alpha = 1°$, 3°, and 5°. Again the variation is linear with zero intercept. The slope of this curve is equal to the right-hand side of equation 3 divided by δ, i.e., the uncorrected pitch-damping moment. Therefore, the variation of predicted pitch-damping moment coefficient is also small across the coning angles investigated.

Although not presented in this report, the pitch-damping force is also easily obtained from this method. Since Magnus and pitch-damping forces are rarely obtained from experimental methods, there was no comparison data to be shown. Obtaining these forces from the CFD is an added benefit of the computational method.

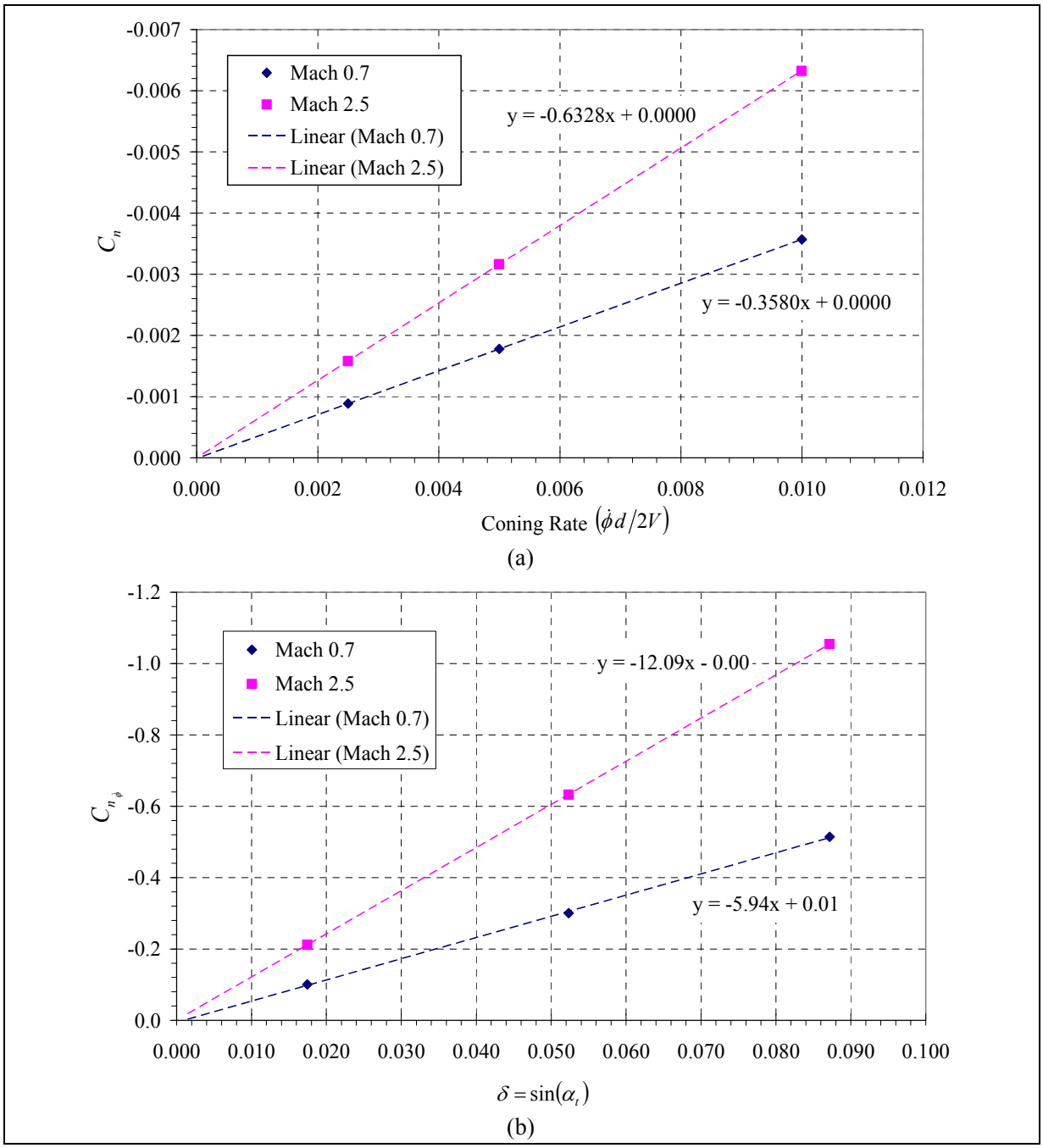

Figure 9. M910 projectile: (a) variation of side moment due to coning with coning rate and (b) variation of side moment slope due to coning with angle of attack.

4.2 U.S. Army-Navy Spinner Rocket

A complete set of static and dynamic coefficients for the ANSR are reported elsewhere (*19*). The roll damping, Magnus moment, and pitch damping are presented here in figures 10 and 11. Note the experimentally determined dynamic derivatives generally have larger errors associated with them than the static coefficients; estimated at ±20% for Magnus and pitch damping, and ±10% for roll damping (*32*). Error bars are not shown in the plots so as to not reduce the clarity of the plots.

The roll damping (figure 10a) compares reasonably well with the experimental data. The roll-damping values were obtained at $\alpha = 2°$; however, C_{lp} was found to be relatively insensitive to angle of attack up to the 5° level for each of the projectiles investigated in this study. Over the Mach number range shown, the CFD values of C_{lp} are under predicted (i.e., larger negative, so damping is over predicted) by about 8%–15%. The trend of decreasing roll damping with Mach number is predicted very well by the CFD.

Figure 10b shows the comparison of predicted and experimental Magnus moment for the three c.g. locations investigated: forward (F), middle (M), and rear (R). The predicted values fall within the data very well for $M \geq 1$. However, the experimental Magnus moment data shows a larger downward trend for $M < 1$ than the predicted values. Note that there are extremely large amounts of scatter in the experimental data at all c.g. locations. Still, there is definitely a larger negative trend in the experimental data than there is in the CFD predictions. As mentioned earlier, there is still an unresolved issue pertaining to the accuracy of steady-state CFD predictions of Magnus in the subsonic and transonic flight regimes.

The ANSR does not exhibit the very large negative Magnus moment indicative of nonlinear effects like the M910, shown in the next section. Weinacht (*33*) demonstrated that the shape of the projectile base is likely the dominant cause of nonlinear Magnus moment. Weinacht showed that replacing a rounded base with a sharp, nearly square base nearly eliminated the nonlinear Magnus of a small-arms projectile. While there is definitely more scatter in the experimental data at $M < 1$, the variation of Magnus moment with angle of attack is still fairly linear (*21*, *34*).

Figure 11 shows the pitch-damping predictions from three different CFD codes and two different methods: steady-state coning (SSC) using CFD++; SSC using Overflow 2 (OF-2); SSC using a PNS code (*1*) (supersonic Mach numbers only); and the transient, planar pitching motion using Overflow 2. The CFD++ calculations were performed using the steady lunar coning motion, while the Overflow 2 and PNS calculations were performed using the steady combined spinning and coning motion. Overflow 2 was also used for the transient planar, constant amplitude sinusoidal pitching motion calculations.

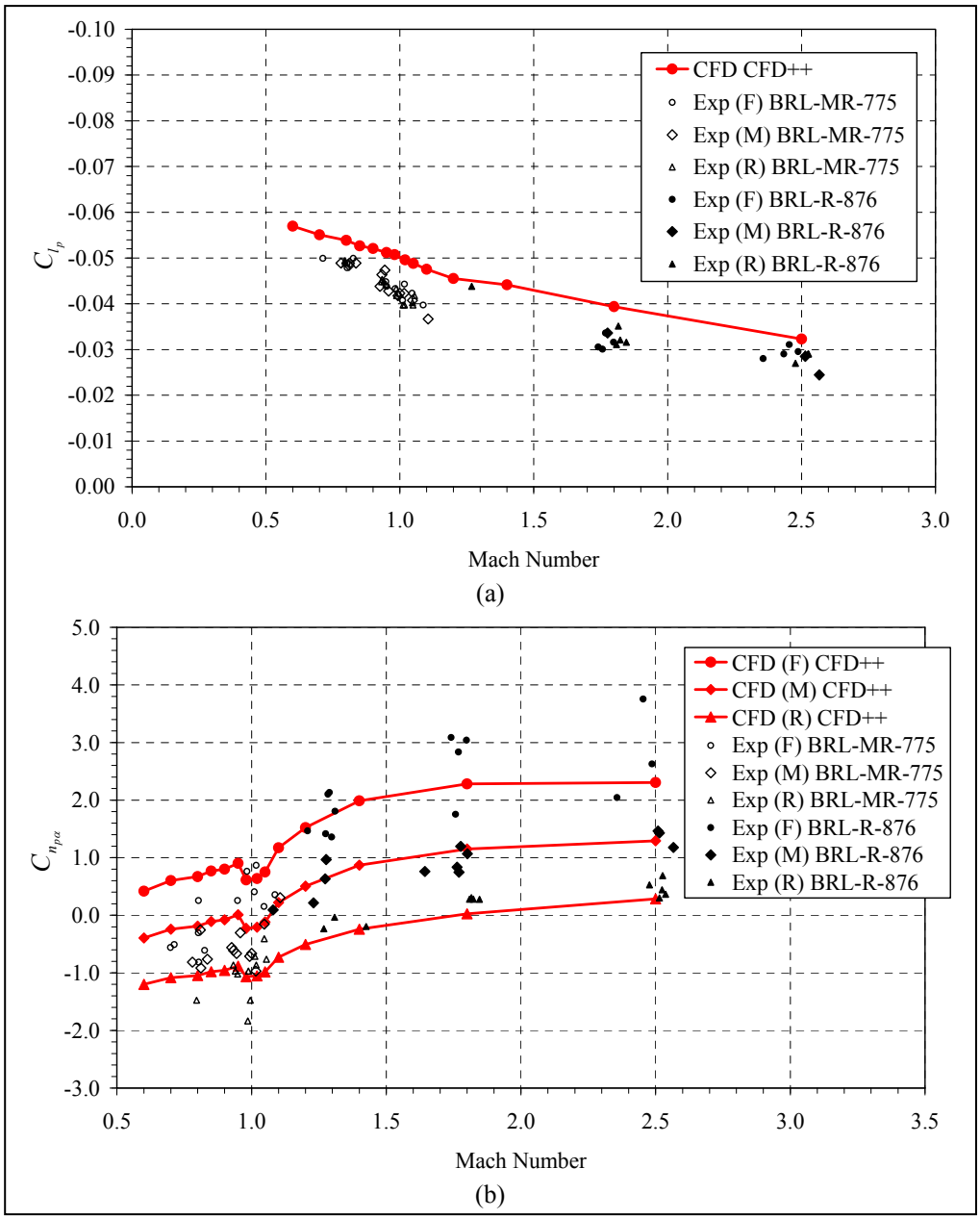

Figure 10. ANSR (a) roll-damping moment and (b) Magnus moment at $\alpha = 2°$.

All four sets of CFD predictions compare to each other extremely well, adding a high degree of confidence to the predictions. The predicted results are in excellent agreement with each other despite differences in the codes and grids applied to obtain the results. The computed results show good agreement with experimental data (*21*, *34*), particularly above the sonic velocity. Results at subsonic velocities show some degree of underprediction of the pitch damping, although there is significantly more scatter in the experimental data at these Mach numbers. Still, the CFD predictions fall within the error bounds, albeit at the ends of the error bounds at the lowest Mach numbers.

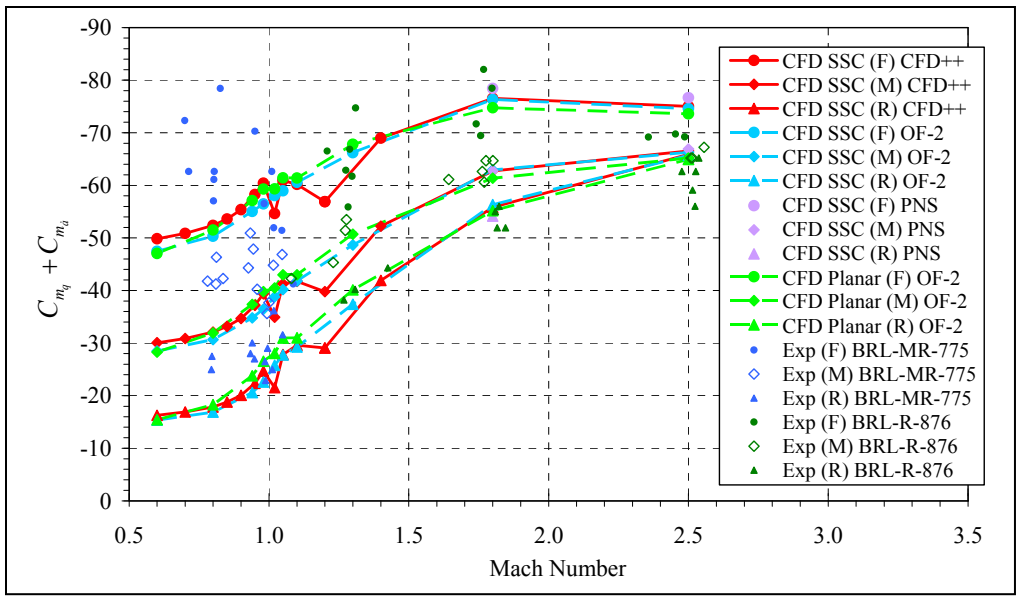

Figure 11. ANSR pitch-damping moment sum.

There are two features of the computed pitch-damping curves that differ between the CFD++ and Overflow 2 calculations. The CFD++ computations show a decrease in the absolute value of pitch damping of about 10%–20% at Mach 1.02. The original level of pitch damping is recovered at Mach 1.05. The Overflow 2 computations show a much smaller change in the value of pitch damping at Mach 1.02. The CFD++ computations show another decrease in the absolute value of pitch damping at Mach 1.2. Unfortunately, Overflow 2 computations were not performed at this same Mach number. The scatter in the experimental data makes it impossible to discern the trend in that data. It is difficult to say what the reasons for the differences are or which is the better computation. Perhaps computing more data points in this narrow Mach number range is warranted.

4.3 The 25-mm M910

The static aerodynamic coefficients, roll damping, and Magnus moments predicted using CFD++ were reported previously (*18*). The roll-damping and Magnus moments are shown in figures 12 and 13, along with the pitch-damping coefficient predictions. The predictions of roll damping (figure 12) compare very well with the experimental data for $M > 1$. At and below Mach 1, the CFD predictions fall at the upper bound of the estimated error in the experimental values (*18*, *35*). The CFD prediction is about 15% higher than the error bound of the group fit point (*18*) just below Mach 1. The C_{lp} values in figure 12 are for $\alpha = 3°$ but the actual value was found insensitive to angle of attack.

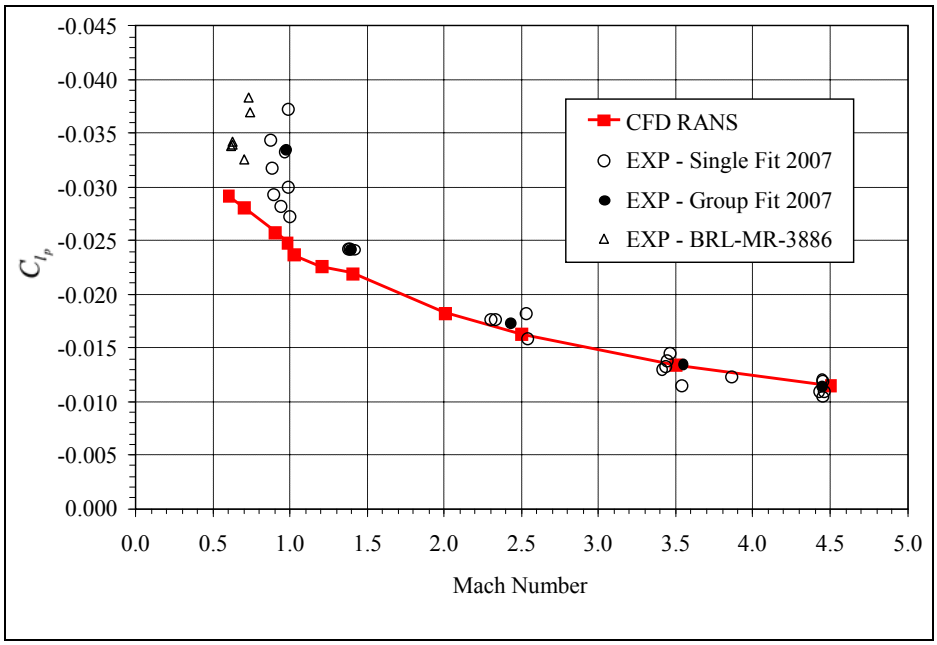

Figure 12. M910 roll-damping moment.

The predictions of Magnus moment, figure 13a, again compare reasonably well in the supersonic region (where the Magnus moment is very near zero). However, the CFD does not predict the large negative nonlinear Magnus moment at the lower Mach numbers. Time-accurate RANS/LES simulations better predicted the lower Magnus moment in the subsonic range, as shown in figure 13a. The magnitude of the Magnus moment did not approach that of the experimental data; however, this result is an indication that transient flow effects may have to be taken into account in the subsonic and transonic flight regimes in order to predict Magnus effects, at least for this projectile shape. The issue of Magnus prediction at lower Mach numbers is more fully addressed elsewhere (*18*, *19*).

The comparison of predicted and experimental pitch-damping moment coefficients are shown in Figure 13b. The CFD predictions fall within the scatter in the experimental data across the Mach number range. The predicted pitch-damping coefficient again shows a dip in the absolute value at Mach 1.02; however, it is only about 4%. The comparison is very good for $M \geq 1$. At $M < 1$, the experimental data (reduced using linear theory methods [35] shows positive values of pitch-damping moment. When the more advanced 6-degree of freedom (6-DOF) reductions were used to reduce the data (single fit 2007 and group fit 2007), the positive pitch-damping moment coefficient is eliminated, though in some cases by holding it fixed at zero. It is generally believed that the pitch-damping moment is not positive, and that small pitch-damping moment coefficients (absolute values <5) are difficult to resolve, especially when nonlinear Magnus moment coefficients are present. The values of cubic Magnus and pitch-damping moment coefficients are coupled and are difficult to separate even when the nonlinear least-squares data

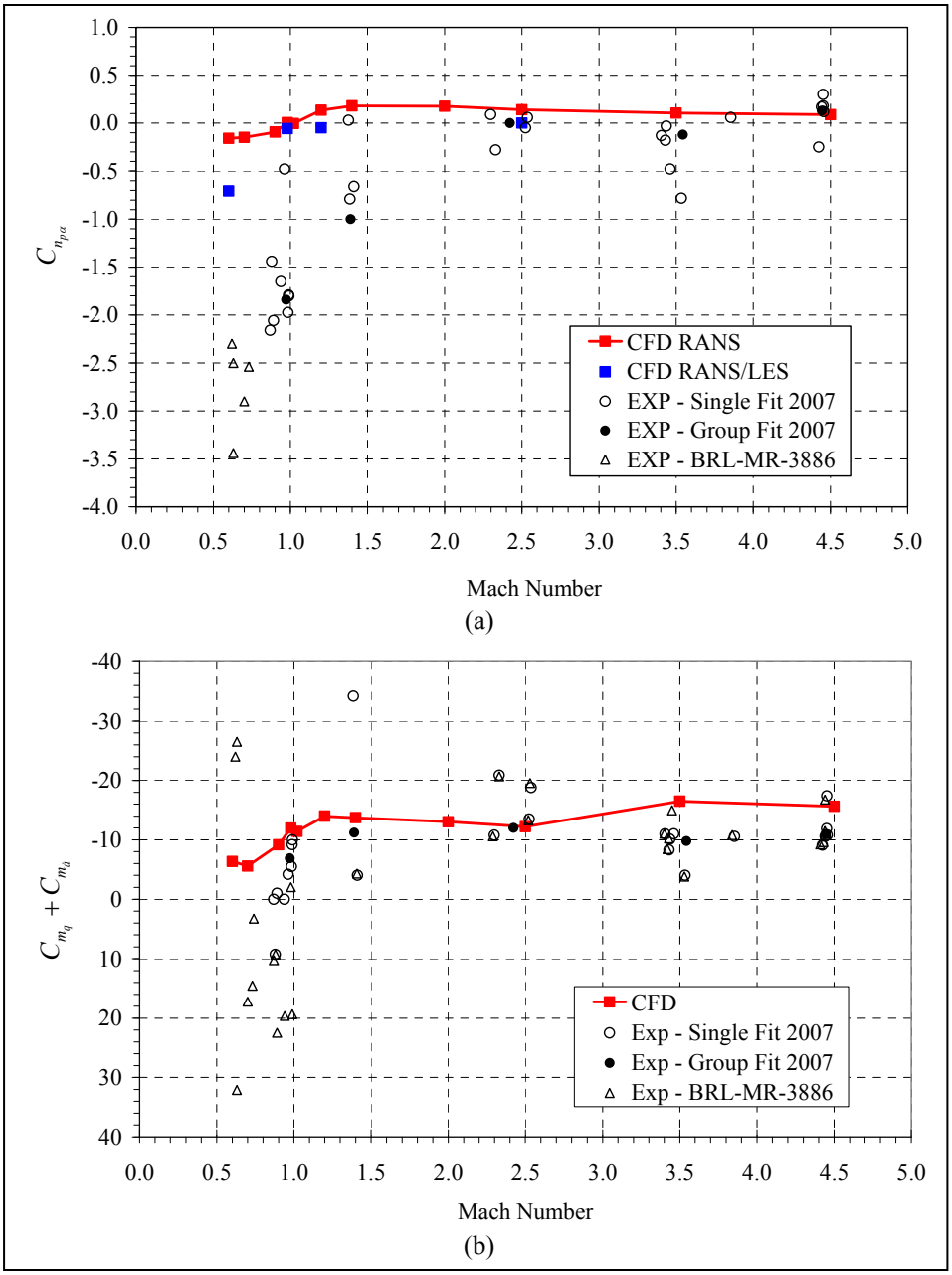

Figure 13. M910 (a) Magnus moment at $\alpha = 3°$ and (b) pitch-damping moment sum.

reduction process (*36*) is used. The question has been raised, and is currently under investigation, that if there are large errors associated with the experimental pitch damping, is the effect on the experimental Magnus moment truly known. One way that this discrepancy in the experimental data reductions has been overcome is to use multiple shots to determine a group fit and use this value fixed in the remainder of the experimental data reductions. The authors have a strong confidence in the CFD predicted values of pitch-damping moment at all Mach numbers. The accuracy of the Magnus predictions at the lower Mach numbers, especially via steady-state

computations, is still at issue. However, we believe some of the experimental nonlinear Magnus data at the lower Mach numbers should also be questioned, especially if accompanied by positive pitch-damping values. The M910 provides a good configuration for the study of nonlinear Magnus and pitch damping and further investigation is planned.

4.4 The 0.50-cal. Projectile

The CFD predictions of the roll-damping, Magnus, and static aerodynamic coefficients for the 0.50-cal. projectile were previously reported (*16*). The roll-damping, pitch-damping moment, and Magnus predictions are shown in figures 14 and 15. The CFD predictions are compared to archival experimental data from the former U.S. Army Ballistic Research Laboratory (BRL).

The prediction of roll damping (figure 14a) shows a decreasing trend with Mach number. Comparisons of the predicted roll-damping moment are made with experimental data from BRL (*30*) and the Defence Research and Development Canada (DRDC) – Valcartier (*37, 38*). The latter set of data includes results from two nominal Mach numbers, 1.5 and 2.4, and shows good agreement with the predicted results. Although the BRL roll-damping data has been used previously as validation data (*16*), further investigation has revealed that the experimental C_{lp} values used in the current data reduction were held fixed based on previous empirical estimates that are inaccurate. The original BRL C_{lp} data has been referenced numerous times in the archival literature without knowledge of the discrepancies. Therefore, care must be taken in the future to not use this original set of data. Unfortunately, no other experimental data was found for $M < 1$. The trend of the CFD C_{lp} values in this range is also closer to that observed for the ANSR and M910 projectiles.

Figure 14b shows the comparison of predicted pitch-damping moment with the experimental data. The DRDC and BRL experimental data generally agree to within the error bounds. The CFD predictions for coning angles of 2° and 5° are shown and they compare very well, differing only at one data point just above Mach 1. Interestingly, predicted values of pitch damping again show a dip in the absolute value just over Mach 1.0. For the 2° coning angle, the reduction is about 22% at Mach 1.04, while for the 5° coning angle, the reduction is about 8% at Mach 1.1. One possibility is that there is a shock interaction effect responsible for the change in pitch damping near Mach 1. The predicted values generally fall within the experimental data for $M > 1$. Near Mach 1 and below the scatter in the experimental data is very large, including positive values of pitch-damping moment. The experimental data also exhibits some positive pitch-damping values in the range $0.6 < M < 1.0$. We believe the CFD predicted values may once again be assumed to be the more reliable values for $M < 1$.

The prediction of Magnus moment at $\alpha = 2°$ is shown in figure 15a. In the supersonic regime, the experimental analyses show that Magnus moment remains approximately constant. The CFD predicts this supersonic trend, although the value is overpredicted for $M < 2.4$. In the subsonic regime, the error in the experimental data is quite large, as well as scattered, so that it is unclear as to what the trends actually are; however, the CFD overpredicts the Magnus moment in this

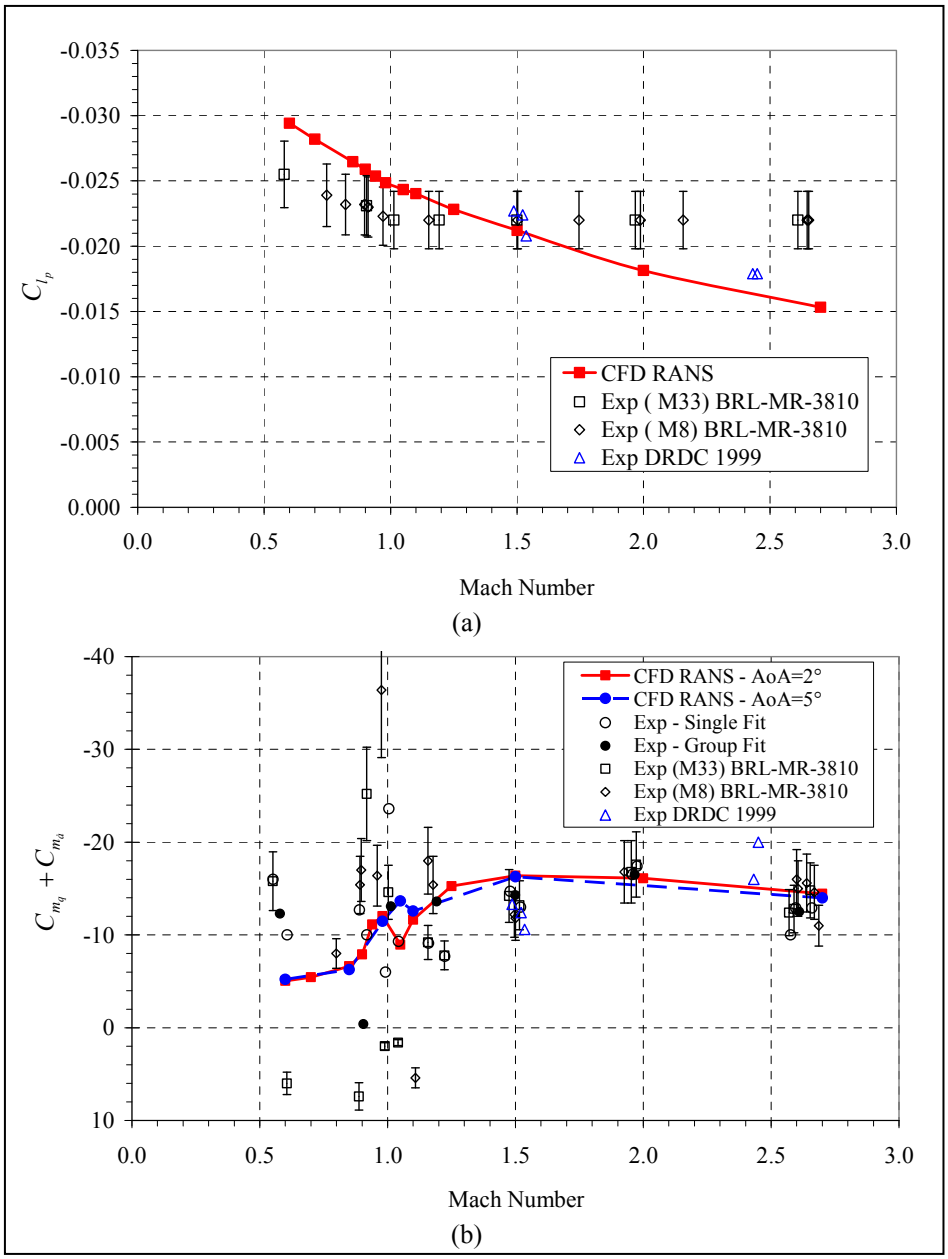

Figure 14. The 0.50-cal. projectile (a) roll-damping moment and (b) pitch-damping moment sum.

regime also. In the transonic regime, the general trend of a peak in Magnus moment is correctly predicted, but again the value is overpredicted. Silton (*16*) indicated that the discrepancy in the Magnus prediction might also be attributable to the lack of engraving in the CFD model. However, in computational and experimental investigations, respectively, Weinacht (*39*) and Silton and Webb (*40*) recently showed that engraving bands have little effect on the Magnus moment at the spin rates used in these studies. Further investigation of the 0.50-cal. Magnus effects using time-accurate RANS/LES simulations is ongoing.

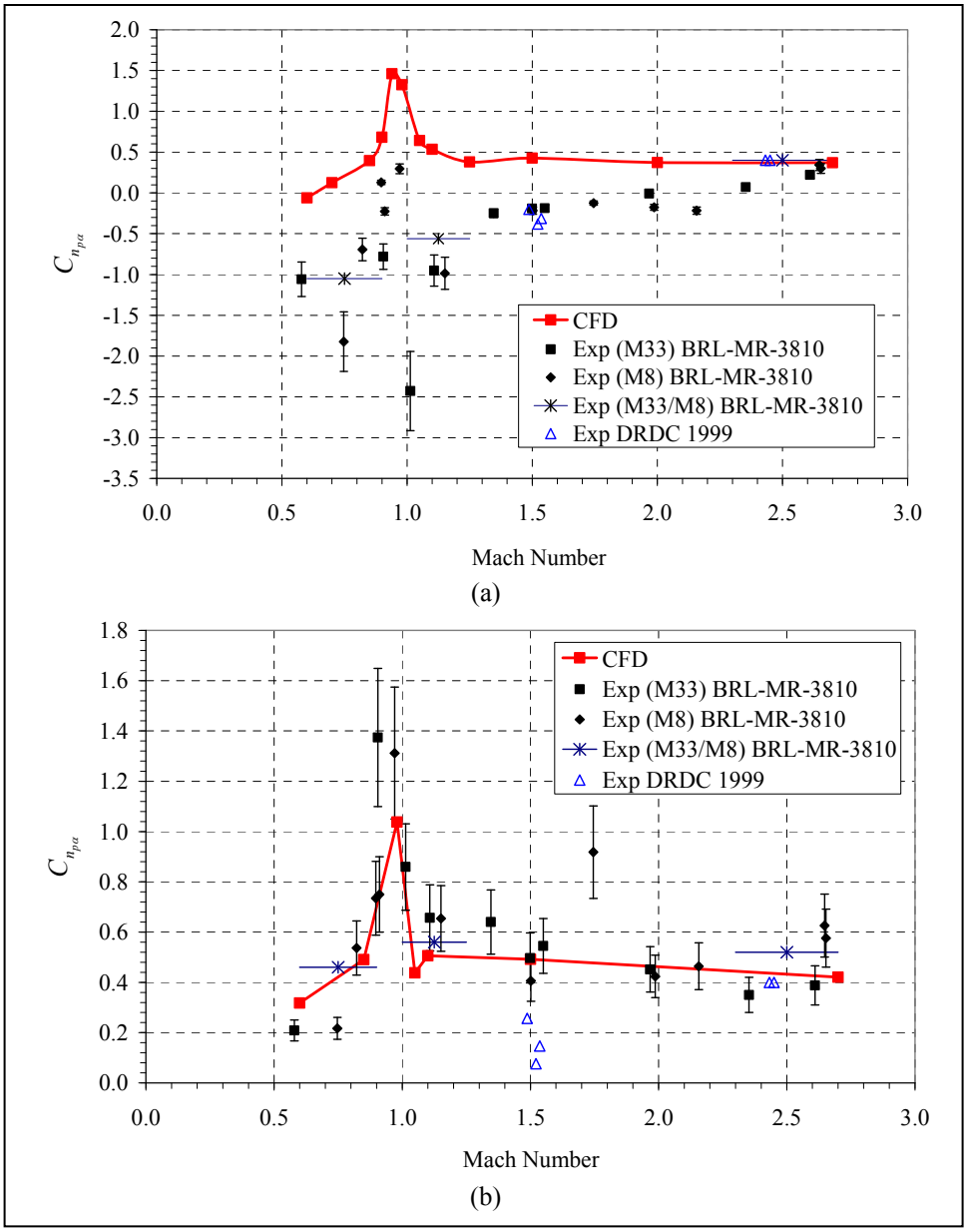

Figure 15. The 0.50-cal. projectile Magnus moment at (a) $\alpha = 2°$ and (b) $\alpha = 2°$.

At $\alpha = 5°$, the data trends in the CFD solution and experimental data appear to agree rather well (figure 15b). The DRDC experimental data at Mach 2.4 is a little lower than the BRL experimental data and CFD predictions. The agreement of the CFD prediction with the experimental data in the supersonic regime is quite good, accurately predicting both trend and magnitude. The CFD accurately predicted the critical behavior in the transonic regime. However, as Mach 1 is approached, the CFD appears to underpredict the Magnus moment, but is close to the error bound on the experimental data. The CFD again overpredicts the Magnus moment in the subsonic regime.

5. Summary and Conclusions

The prediction of the dynamic stability derivatives, roll-damping, Magnus, and pitch-damping moments were presented for three spin-stabilized projectiles. Roll damping was shown to be adequately predicted via steady-state CFD methods. The prediction of Magnus moment in the supersonic flight regime was also shown to be adequate using steady-state methods. However, in the subsonic and transonic flight regime the accuracy of CFD prediction of Magnus moment is not clearly defined. The CFD usually predicted the decreasing trend of Magnus moment with decreasing Mach number; however, the steady-state CFD overpredicted the value of Magnus moment at the lower Mach numbers. Time-accurate RANS/LES simulations improved the CFD predictions of Magnus moment for the M910 projectile, but had little effect on the Magnus moment predicted for the ANSR. The prediction of Magnus issue is still under investigation.

A primary focus of this report was the demonstration of the capability to predict the pitch-damping moment via steady-state CFD methods. The pitch-damping moment predicted by the CFD compared very well with available experimental data for the three projectiles investigated. The only discrepancy was at the lower Mach numbers, where the experimental data showed a large level of scatter and was sometimes accompanied by unlikely positive values of pitch-damping moment. Therefore, the CFD prediction can probably be assumed the more accurate value at the lower Mach numbers.

The prediction of pitch damping of the ANSR was demonstrated by several CFD codes, two different steady-state CFD methods, and a time-accurate planar pitching motion method. All methods compared extremely well to each other and to the experimental data.

Roll-damping and pitch-damping CFD predictions were found to be very good across the Mach number ranges investigated. The limitations of small angle of attack and low spin rates for the pitch-damping calculations do not hinder the usefulness of the method since they are adequate for most cases. The accuracy of the Magnus moment predictions was very good in the supersonic flight regime but varied in the subsonic and transonic flight regimes. The best comparison of Magnus moment prediction with experimental data was found for the square-base ANSR configurations, which did not have highly nonlinear Magnus moments. These results demonstrate that steady-state CFD methods can be adequate to predict the dynamic derivatives of spin-stabilized projectiles. Time-accurate methods need be resorted to for only those cases necessary, making the most efficient use of computational resources.

6. References

1. Weinacht, P.; Sturek, W. B.; Schiff, L. B. Navier-Stokes Predictions of Pitch Damping for Axisymmetric Projectiles. *J. Spacecraft Rockets* **1997**, *34* (6), 753–761.

2. Weinacht, P. Navier-Stokes Predictions of the Individual Components of the Pitch-Damping Sum. *J. Spacecraft Rockets* **1998**, *35* (5), 598–605.

3. Weinacht, P. Prediction of Pitch-Damping of Projectiles at Low Supersonic and Transonic Velocities. AIAA-98-0395; *Proceedings of the 36th Aerospace Sciences Meeting,* Reno, NV, 12–15 January 1998.

4. Weinacht, P.; Sturek, W. B. Navier-Stokes Predictions of Pitch Damping of Finned Projectiles Using Steady Coning Motion. AIAA-90-3088; *Proceedings of the 8th AIAA Aerodynamics Conference,* Portland, OR, 20–22 August 1990.

5. Sturek, W. B.; Nietubicz, C. J.; Sahu, J.; Weinacht, P. Applications of Computational Fluid Dynamics to the Aerodynamics of Army Projectiles. *J. Spacecraft Rockets* **1994**, *31* (2), 186–199.

6. Weinacht, P. Projectile Performance, Stability, and Free-Flight Motion Prediction Using Computational Fluid Dynamics. *J. Spacecraft Rockets* **2004**, *4* (2), 257–263.

7. Park, S. H.; Kim, Y.; Kwon, J. H. Prediction of Damping Coefficients Using the Unsteady Euler Equations. *J. Spacecraft Rockets* **2003**, *40* (3), 356–362.

8. Park, S. H.; Kwon, J. H. Navier-Stokes Computations of Stability Derivatives for Symmetric Projectiles. AIAA-2004-0014; *Proceedings of the 42nd Aerospace Sciences Meeting,* Reno, NV, 5–8 January 2004.

9. Oktay, E.; Akay, H. U. CFD Predictions of Dynamic Derivatives for Missiles. AIAA-2002-0276; *Proceedings of the 40th Aerospace Sciences Meeting,* Reno, NV, 14–17 January 2002.

10. Stalnaker, J. F.; Robinson, M. A. Computations of Stability Derivatives of Spinning Missiles Using Unstructured Cartesian Meshes. AIAA-2002-2802; *Proceedings of the 20th AIAA Aerodynamics Conference,* St. Louis, MO, 24–26 June 2002.

11. Sahu, J. Numerical Computations of Dynamic Derivatives of a Finned Projectile Using a Time-Accurate CFD Method. AIAA-2007-6581; *Proceedings of the AIAA Atmospheric Flight Mechanics Conference,* Hilton Head, SC, 20–23 August 2007.

12. Sahu, J. Time-Accurate Computations of Free-Flight Aerodynamics of a Spinning Projectile with Flow Control. AIAA-2006-6006; *Proceedings of the AIAA Atmospheric Flight Mechanics Conference,* Keystone, CO, 21–24 August 2006.

13. Sturek, W. B.; Schiff, L. B. Computations of the Magnus Effect for Slender Bodies in Supersonic Flow. *AIAA J.* **1982**, *20* (12), 1724–1731.

14. Nietubicz, C. J.; Sturek, W. B.; Heavey, K. R. *Computations of Projectile Magnus Effect at Transonic Velocities;* BRL-TR-02515; U.S. Army Ballistics Research Laboratory: Aberdeen Proving Ground, MD, August 1983.

15. Sahu, J. *Transonic Navier-Stokes Computations for a Spinning Body of Revolution;* BRL-TR-3265; U.S. Army Ballistics Research Laboratory: Aberdeen Proving Ground, MD, September 1991.

16. Silton, S. I. Navier-Stokes Computations for a Spinning Projectile from Subsonic to Supersonic Speeds. *J. Spacecraft Rockets* **2005**, *42* (2), 223–231.

17. DeSpirito, J.; Heavey, K. R. CFD Computation of Magnus Moment and Roll Damping Moment of a Spinning Projectile. AIAA-2004-4713; *Proceedings of the AIAA Atmospheric Flight Mechanics Conference,* Providence, RI, 16–19 August 2004.

18. DeSpirito, J.; Plostins, P. CFD Prediction of M910 Projectile Aerodynamics: Unsteady Wake Effect on Magnus Moment. AIAA-2007-6580; *Proceedings of the AIAA Atmospheric Flight Mechanics Conference,* Hilton Head, SC, 20–23 August 2007.

19. DeSpirito, J. CFD Prediction of Magnus Effect in Subsonic to Supersonic Flight. AIAA-2008-0427; *Proceedings of the 46th Aerospace Sciences Meeting,* Reno, NV, 7–10 January 2008.

20. Fluent, Inc. *Fluent 6.3 User's Guide*; Vol. 2; Lebanon, NH, 2006.

21. Schmidt, L. E.; Murphy, C. H. *The Aerodynamic Properties of the 7-Caliber Army-Navy Spinner Rocket in Transonic Flight;* BRL-MR-775; U.S. Army Ballistics Research Laboratory: Aberdeen Proving Ground, MD, March 1954.

22. Metacomp Technologies, Inc. *CFD^{++} User's Manual*; Agoura Hills, CA, 2006.

23. Renze, K. J.; Buning, P. G.; Ragagopalan, R. G. A Comparative Study of Turbulence Models for Overset Grids. AIAA-92-0437; *Proceedings of the 30th Aerospace Sciences Meeting,* Reno, NV, 6–9 January 1992.

24. Meakin, R. L. A New Method for Establishing Inter-Grid Communication Among Systems of Overset Grids. AIAA-91-1586; *Proceedings of the 10th AIAA Computational Fluid Dynamics Conference,* Honolulu, HI, 24–27 June 1991.

25. Chan, W. M. The Overgrid Interface for Computational Simulations on Overset Grids. AIAA-2002-3188; *Proceedings of the 32nd AIAA Fluid Dynamics Conference,* St. Louis, MO, 24–26 June 2002.

26. Baldwin, B. S.; Barth, T. J. A One-Equation Turbulence Transport Model, for High Reynolds Number Wall-Bounded Flows. AIAA-91-610; *Proceedings of the 29th Aerospace Sciences Meeting,* Reno, NV, 7–10 January 1991.

27. Park, S. H.; Kwon, J. H. Navier-Stokes Computation of Pitch-Damping Coefficients Using Steady Coning Motion. *J. Spacecraft Rockets* **2004**, *41* (5), 754–761.

28. Murman, S. M.; Chan, W. M.; Aftosmis, M. J.; Meakin, R. L. An Interface for Specifying Rigid-Body Motions for CFD Applications. AIAA-2003-1237; *Proceedings of the 41st Aerospace Sciences Meeting,* Reno, NV, 6–9 January 2003.

29. Chan, W. M.; Buning, P. G. *User's Manual for FOMOCO Utilities – Force and Moment Computation Tools for Overset Grids*; NASA TM-110408; National Aeronautics and Space Administration: Washington, DC, July 1996.

30. McCoy, R. L. *The Aerodynamic Characteristics of .50 Ball, M33, API, M8, and APIT, M20 Ammunition;* BRL-MR-3810; U.S. Army Ballistics Research Laboratory: Aberdeen Proving Ground, MD, January 1990.

31. Pointwise, Inc. *GRIDGEN Users Manual*; Bedford, TX, 2006.

32. Arrow Tech Associates. *ARFDAS 4.11 User's Guide*; South Burlington, VT, 1997.

33. Weinacht, P. Characterization of Small-Caliber Ammunition Performance Using a Virtual Wind Tunnel Approach. AIAA-2007-6579; *Proceedings of the AIAA Atmospheric Flight Mechanics Conference,* Hilton Head, SC, 20–23 August 2007.

34. Murphy, C. H.; Schmidt, L. E. *The Effect of Length on the Aerodynamic Characteristics of Bodies of Revolution in Supersonic Flight;* BRL-R-876; U.S. Army Ballistics Research Laboratory: Aberdeen Proving Ground, MD, August 1953.

35. Plostins, P.; McCoy, R. L.; Wagoner, B. A. *Aeroballistic Performance of the 25 mm M910 TPDS-T Range Limited Training Projectile;* BRL-MR-3886; U.S. Army Ballistics Research Laboratory: Aberdeen Proving Ground, MD, January 1991.

36. McCoy, R. L. *Modern Exterior Ballistics: The Launch and Flight Dynamics of Symmetric Projectiles*; Schiffer Books: Atglen, PA, 1998, 273–298.

37. The Technical Cooperation Program. http://www.dtic.mil/ttcp/ (accessed 28 May 2008).

38. Dupuis, A. D.; Bernier, A.; Hathaway, W. *Data Compendium of the Free-Flight Aerodynamic Characteristics of 0.50 cal. Configurations for Range Limited Application at Supersonic Speeds;* DREV-TR-1999-060; Defence Research and Development Canada: Valcartier, CA, November 1999.

39. Weinacht, P. Validation and Prediction of the Effect of Rifling Grooves on Small-Caliber Ammunition Performance. AIAA-2006-6010; *Proceedings of the AIAA Atmospheric Flight Mechanics Conference,* Keystone, CO, 21–24 August 2006.

40. Silton, S.; Webb, D. Experimental Determination of the Effect of Rifling Grooves on the Aerodynamics of Small Caliber Projectiles. AIAA-2006-6009; *Proceedings of the AIAA Atmospheric Flight Mechanics Conference,* Keystone, CO, 21–24 August 2006.

List of Symbols, Abbreviations, and Acronyms

C_{l_p}	=	roll-damping coefficient
C_m	=	pitching moment coefficient
$C_{m_q} + C_{m_{\dot{\alpha}}}$	=	pitch-damping moment coefficient sum
C_{m_α}	=	slope of pitching moment coefficient with angle of attack
C_{N_α}	=	slope of normal force coefficient with angle of attack
C_n	=	side moment coefficient
$C_{n_{p\alpha}}$	=	slope of Magnus moment coefficient with angle of attack
$C_{n_{\dot{\phi}}}$	=	slope of side moment coefficient with coning rate
d, D	=	missile base diameter, m
k	=	turbulence kinetic energy, m^2/s^2
M	=	Mach number
p	=	projectile spin rate, radians/s, in nonrolling coordinate frame
q_∞	=	dynamic pressure, $\frac{1}{2} \rho V^2$, N/m^2
R	=	undamped eddy viscosity, $\pi d^2/4$, m^2/s
S	=	projectile cross-sectional area, m^2
t	=	time, s
V	=	free stream velocity, m/s
x, y, z	=	axial, horizontal, and vertical body axes
x_{cg}	=	center of gravity location
x_{cp}	=	normal force center of pressure location, $x_{cg} - (C_{m_\alpha} / C_{N_\alpha})$
α	=	vertical component of angle of attack in nonrolling coordinates
$\dot{\alpha}$	=	time rate of change of angle of attack, s^{-1}
α_0	=	amplitude of angle of attack for forced planar pitching motion

$\dot{\alpha}_0$	=	frequency of forced planar pitching motion, s^{-1}
α_t	=	total angle of attack, $\sqrt{\alpha^2 + \beta^2}$
β	=	horizontal component of angle of attack in nonrolling coordinates
γ	=	cosine of total angle of attack
δ	=	sine of total angle of attack
ε	=	turbulence dissipation rate, m^2/s^3
ρ	=	density, kg/m^3
$\dot{\phi}$	=	coning rate of projectile, radians/s
ω	=	spin rate in coning reference frame, radians/s
Ω	=	coning rate of projectile, nondimensionalized by $2V/d$

NO. OF
COPIES ORGANIZATION

1 (PDF only) DEFENSE TECHNICAL INFORMATION CTR
DTIC OCA
8725 JOHN J KINGMAN RD
STE 0944
FORT BELVOIR VA 22060-6218

1 US ARMY RSRCH DEV & ENGRG CMD
SYSTEMS OF SYSTEMS INTEGRATION
AMSRD SS T
6000 6TH ST STE 100
FORT BELVOIR VA 22060-5608

1 DIRECTOR
US ARMY RESEARCH LAB
IMNE ALC IMS
2800 POWDER MILL RD
ADELPHI MD 20783-1197

1 DIRECTOR
US ARMY RESEARCH LAB
AMSRD ARL CI OK TL
2800 POWDER MILL RD
ADELPHI MD 20783-1197

1 DIRECTOR
US ARMY RESEARCH LAB
AMSRD ARL CI OK T
2800 POWDER MILL RD
ADELPHI MD 20783-1197

ABERDEEN PROVING GROUND

1 DIR USARL
AMSRD ARL CI OK TP (BLDG 4600)

NO. OF COPIES ORGANIZATION

1 AIR FORCE RESEARCH
LABORATORY
AFRL MNAV
G ABATE
101 W EGLIN BLVD STE 333
EGLIN AFB FL 32542-6810

3 US ARMY AMRDEC
AMSAM RD SS AT
R W KRETZSHMAR
L AUMAN
E VAUGHN
REDSTONE ARSENAL AL 35898-5000

1 CDR US ARMY
TACOM ARDEC
SFAE AMO MAS
C GRASSANO
BLDG 354
PICATINNY ARSENAL NJ 07806-5000

1 COMMANDER
US ARMY TACOM ARDEC
AMSRD AAR AEM C
P MAGNOTTI
BLDG 61S
PICATINNY ARSENAL NJ
07806-5000

1 COMMANDER
US ARMY TACOM ARDEC
SFAE AMO CAS
M MORATZ
BLDG 171A
PICATINNY ARSENAL NJ
07806-5000

3 COMMANDER
US ARMY ARDEC
ASMRD AAR AEP E
D CARLUCCI
I MEHMEDAGIC
C STOUT
BLDG 94
PICATINNY ARSENAL NJ 07806-5000

1 COMMANDER
US ARMY ARDEC
ASMRD AAR AEP E
C KESSLER
BLDG 3022
PICATINNY ARSENAL NJ 07806-5000

NO. OF COPIES ORGANIZATION

1 COMMANDER
US ARMY ARDEC
AMSRD AAR MEM A
W SU
BLDG 94
PICATINNY ARSENAL NJ 07806-5000

13 COMMANDER
US ARMY ARDEC
AMSRD AAR AEM A
S CHUNG
A FARINA
J GRAU
S HAN
W KOENIG
C LIVECCHIA
G MALEJKO
W TOLEDO
R TROHANOWSKY
E VAZQUEZ
C WILSON
B WONG
L YEE
BLDG 95
PICATINNY ARSENAL NJ 07806-5000

1 US ARMY TACOM ARDEC
CCAC
AMSRD AAR AEM J
G FLEMING
BLDG 65N
PICATINNY ARSENAL NJ 07806-5000

1 US ARMY TACOM ARDEC
CCAC
AMSTA AR CCL B
J MIDDLETON
BLDG 65N
PICATINNY ARSENAL NJ 07806-5000

1 US ARMY TACOM ARDEC
ASIC PRGM INTEGRATION OFC
J A RESCH
BLDG 1
PICATINNY ARSENAL NJ 07801

1 US ARMY TACOM ARDEC
AMSRD AAR AEW M(D)
M D MINISI
BLDG 65N
PICATINNY ARSENAL NJ 07806-5000

NO. OF COPIES ORGANIZATION

1 US ARMY TACOM ARDEC
AMSRD AR CCL C
S SPICKERT-FULTON
BLDG 65N
PICATINNY ARSENAL NJ 07806-5000

1 US ARMY TACOM ARDEC
AMSRD AAR AEM T
M NICOLICH
BLDG 65S
PICATINNY ARSENAL NJ 07806-5000

1 US ARMY TACOM ARDEC
AMSRD AAR AEM S
S J MUSALLI
BLDG 65S
PICATINNY ARSENAL NJ 07806-5000

1 US ARMY ARDEC
AMSRD AAR AEM M
V GONSALVES
BLDG 61S
PICATINNY ARSENAL NJ 07806-5000

1 US ARMY ARDEC
AMSRD AAR AEM S
D DIEDALIS
BLDG 162N
PICATINNY ARSENAL NJ 07806-5000

1 US ARMY ARDEC
AMSRD AAR AEM I
D CONWAY
BLDG 65N
PICATINNY ARSENAL NJ 07806-5000

1 US ARMY ARDEC
AMSTA DSA SA
A CLINE
BLDG 151
PICATINNY ARSENAL NJ 07806-5000

2 PM MAS
SFAE AMO MAS SMC
F HANZL
P RIGGS
BLDG 354
PICATINNY ARSENAL NJ 07806-5000

NO. OF COPIES ORGANIZATION

1 PM MAS
SFAE AMO MAS MC
G DEROSA
BLDG 354
PICATINNY ARSENAL NJ 07806-5000

1 AEROPREDICTION INC
F MOORE
9449 GROVER DR STE 201
KING GEORGE VA 22485

1 UNIVERSITY OF ILLINOIS
AERO ENG DEPT
J C DUTTON
306F TALBOT LAB
104 S WRIGHT ST
URBANA IL 61801

2 ATK TACTICAL SYS DIV
ALLEGANY BALLISTICS LAB
D J LEWIS
J S OWENS
210 STATE RTE 956
ROCKET CENTER WV 26726

1 ALLIANT TECHSYSTEMS INC
R H DOHRN
MN07 LW54
5050 LINCOLN DR
EDINA MN 55436

1 ALLIANT TECHSYSTEMS
B BECKER
5050 LINCOLN DR
EDINA MN 55340-1097

2 ALLIANT TECHSYSTEMS INC
C AAKHUS
MN07 LW54
D KAMDAR
MN07 LW54
5050 LINCOLN DR
EDINA MN 55436

1 ALLIANT TECHSYSTEMS INC
M JANTSCHER
MN07 LW54
5050 LINCOLN DR
EDINA MN 55436

NO. OF
COPIES ORGANIZATION

3 ATK LAKE CITY
K ENLOW
D MANSFIELD
J WESTBROOK
PO BOX 1000
INDEPENDENCE MO 64051-1000

1 SCIENCE APPLICATIONS INTL CORP
J NORTHRUP
8500 NORMANDALE LAKE BLVD
STE 1610
BLOOMINGTON MN 55437

2 GOODRICH ACTUATION SYSTEMS
T KELLY
P FRANZ
100 PANTON RD
VERGENNES VT 05491

2 ARROW TECH ASSOC
W HATHAWAY
J WHYTE
1233 SHELBURNE RD STE D8
SOUTH BURLINGTON VT 05403

1 KLINE ENGINEERING CO INC
R W KLINE
27 FREDON GREENDEL RD
NEWTON NJ 07860-5213

1 SIERRA BULLETS
P DALY
1400 W HENRY ST
SEDALIA MO 65302-0818

1 GEORGIA INST TECH
DEPT AEROSPACE ENGR
M COSTELLO
270 FERST ST
ATLANTA GA 30332

ABERDEEN PROVING GROUND

20 DIR USARL
AMSRD WM
J SMITH
AMSRD ARL WM B
M ZOLTOSKI
J NEWILL
C CANDLAND
AMSRD ARL WM BA
D LYON

NO. OF
COPIES ORGANIZATION

AMSRD ARL WM BC
I CELMINS
M CHEN
G COOPER
J DESPIRITO
F FRESCONI
B GUIDOS
K HEAVEY
B HOWELL
G OBERLIN
J SAHU
S SILTON
P WEINACHT
AMSRD ARL BD
B FORCH
AMSRD ARL BF
W OBERLE
AMSRD ARL VT UV
M BUNDY

NO. OF
COPIES ORGANIZATION

1 DSTL BEDFORD
T BIRCH
BLDG 115 RM 125
BEDFORD TECHNOLOGY PARK
BEDFORD
MK44 2FQ
UK

3 DEFENCE RESEARCH AND
DEVELOPMENT CANADA –
VALCARTIER
F LESAGE
D CORRIVEAU
N HAMEL
2459 PIE-XI BLVD NORTH
VAL-BELAIR (QC) G3J1X5
CANADA

INTENTIONALLY LEFT BLANK.